

This work was written as part of one of the author's official duties as an Employee of the United States Government and is therefore a work of the United States Government. In accordance with 17 U.S.C. 105, no copyright protection is available for such works under U.S. Law.

Public Domain Mark 1.0













<https://creativecommons.org/publicdomain/mark/1.0/>

Access to this work was provided by the University of Maryland, Baltimore County (UMBC) ScholarWorks@UMBC digital repository on the Maryland Shared Open Access (MD-SOAR) platform.

Please provide feedback

Please support the ScholarWorks@UMBC repository by emailing scholarworks-group@umbc.edu and telling us what having access to this work means to you and why it's important to you. Thank you.

Performance of a Broad-Band, High-Resolution, Transition-Edge Sensor Spectrometer for X-ray Astrophysics

Stephen J. Smith , Joseph S. Adams, Simon R. Bandler, Sophie Beaumont , James A. Chervenak, Edward V. Denison, William B. Doriese , Malcolm Durkin , Fred M. Finkbeiner , Joseph W. Fowler , Gene C. Hilton, Ruslan Hummatov , Kent D. Irwin, Richard L. Kelley, Caroline A. Kilbourne , Maurice A. Leutenegger, Antoine R. Miniussi , Frederick S. Porter, Carl D. Reintsema , John E. Sadleir, Kazuhiro Sakai , Daniel S. Swetz, Joel N. Ullom, Leila R. Vale, Nicholas A. Wakeham, Edward J. Wassell , and Michael C. Witthoef

Abstract—Future X-ray astrophysics experiments require multiplexed readout of high fill-factor, kilo-pixel arrays of transition-edge sensors (TESs), with very high spectral resolution over a broad range of energies. In this paper we report on a prototype kilo-pixel array of Mo/Au TESs readout with 8-column by 32-row time-division multiplexing (TDM). This system is being used to demonstrate the critical detector and readout technology for ESA's Athena X-IFU, and when complete will be used in laboratory astrophysics experiments. Our array and TDM readout have demonstrated a combined full-width-at-half-maximum energy resolution, including > 200 pixels, of: 1.95 eV for Ti-K α (4.5 keV), 1.97 eV for Mn-K α (5.9 keV), 2.16 eV for Co-K α (6.9 keV), 2.33 eV for Cu-K α (8 keV), 3.26 eV for Br-K α (11.9 keV). The 1 sigma statistical errors are ≤ 0.01 eV for all spectra. These results meet the broad-band resolution requirements for X-IFU with margin.

Index Terms—X-ray spectroscopy, imaging array, multiplexed readout, transition-edge sensor, Athena space telescope.

Manuscript received November 30, 2020; revised February 18, 2021; accepted February 21, 2021. Date of publication February 24, 2021; date of current version March 23, 2021. (Corresponding author: Stephen J. Smith.)

Stephen J. Smith, Joseph S. Adams, Simon R. Bandler, Sophie Beaumont, James A. Chervenak, Fred M. Finkbeiner, Ruslan Hummatov, Richard L. Kelley, Caroline A. Kilbourne, Maurice A. Leutenegger, Antoine R. Miniussi, Frederick S. Porter, John E. Sadleir, Kazuhiro Sakai, Nicholas A. Wakeham, Edward J. Wassell, and Michael C. Witthoef are with the National Aeronautics and Space Administration, Goddard Space Flight Center, Greenbelt, MD 20771 USA (e-mail: stephen.j.smith@nasa.gov; joseph.s.adams@nasa.gov; simon.r.bandler@nasa.gov; sophie.beaumont@nasa.gov; james.a.chervenak@nasa.gov; fred.m.finkbeiner@nasa.gov; ruslan.hummatov@nasa.gov; richard.l.kelley@nasa.gov; caroline.a.kilbourne@nasa.gov; maurice.a.leutenegger@nasa.gov; aminius@umbc.edu; frederick.s.porter@nasa.gov; john.e.sadleir@nasa.gov; kazuhiro.sakai@nasa.gov; nwakeham@umbc.edu; edward.wassell@nasa.gov; michael.c.witthoef@nasa.gov).

Edward V. Denison, William B. Doriese, Malcolm Durkin, Joseph W. Fowler, Gene C. Hilton, Carl D. Reintsema, Daniel S. Swetz, Joel N. Ullom, and Leila R. Vale are with the National Institute of Standards and Technology, Boulder, CO 80305 USA (e-mail: ed.denison@nist.gov; william.doriese@nist.gov; malcolm.durkin@nist.gov; joe.fowler@nist.gov; gene.hilton@nist.gov; carl.reintsema@nist.gov; daniel.swetz@nist.gov; joel.ullom@nist.gov; leila.vale@nist.gov).

Kent D. Irwin is with the Stanford University, Stanford, CA 94305 USA (e-mail: irwin@stanford.edu).

Color versions of one or more figures in this article are available at <https://doi.org/10.1109/TASC.2021.3061918>.

Digital Object Identifier 10.1109/TASC.2021.3061918

I. INTRODUCTION

THE Advanced Telescope for High Energy Astrophysics (Athena) is an ESA led X-ray telescope due to be launched in the early 2030's [1]. Athena was chosen to address the science theme, 'The Hot and Energetic Universe' and will answer questions related to the chemical and physical properties of hot plasmas in the Universe. The X-ray Integral Field Unit (X-IFU) is an instrument on Athena, with a field-of-view of 5 arcminutes, that will provide high-resolution, imaging spectroscopy (2.5 eV for energies up to 7 keV) over the soft X-ray energy range (0.3-12 keV). The X-IFU will use a close-packed microcalorimeter array of 3168 Mo/Au transition-edge sensors (TESs), under development at NASA Goddard Space Flight Center [2]. TESs are superconducting thin film thermistors that are operated (at ~ 90 mK) in the highly temperature sensitive transition region between the superconducting and normal states. Due to the limitations on spacecraft mass and power, the X-IFU array requires a multiplexed readout scheme. The preferred readout approach for X-IFU is time division multiplexing (TDM) developed at NIST (Boulder, CO) [3], [4]. TDM is a mature readout scheme that has been fielded in many laboratory instruments [3] and flown on a sounding rocket experiment [5].

In TDM, each DC-biased TES is inductively coupled to its own superconducting quantum interference device (SQUID) ammeter. Each first stage SQUID (SQ1) 'row' is activated in-turn and measures the signal from its corresponding TES. The SQ1 outputs in a given 'column' are amplified by a second stage SQUID series array (SAA) [6] and room temperature amplifier. To linearize the SQUID output and increase the dynamic range, the circuit is operated in a digitally fed-back, flux locked loop (FLL). Further details of the TDM architecture can be found in [3], [4]. The current TDM baseline for X-IFU is 96 columns each with 34 rows (including 33 science pixels and 1 ohmic resistor for independently tracking the gain of the readout chain.)

Over the past 5 years, improvements to the TES pixel design and the TDM architecture have enabled significant improvements in performance. In 2018 we carried out a series of demonstrations using a prototype X-IFU kilo-pixel array and TDM readout components. This experiment was instrumented to read out 8-columns by 32-rows. Initially, this system was in a 'box-of-chocolates' configuration to study different TDM

design optimizations on the different physical columns [7]. At that time the X-IFU baseline was 40-rows per column. The 32-row system was used to simulate 40-row TDM by measuring the 32 physically distinct rows, with measurements repeated on the last row 8 more times. In a 3-column by “40-row” demonstration, we were able to achieve a full-width-at-half-maximum (FWHM) energy resolution of $\Delta E_{\text{FWHM}} = (2.40 \pm 0.01)$ eV at an energy of 6.9 keV [7]. Since then, the multiplexer chips have been further optimized specifically for X-IFU and the system has been reconfigured to have identical TDM chips populating all 8 columns. Once complete, this 252-pixel instrument will be deployed at the Lawrence Livermore National Laboratory (LLNL), Electron Beam Ion Trap (EBIT) facility as part of our laboratory astrophysics program [8], [9]. The study of highly ionized plasmas in controlled laboratory conditions provides essential input to atomic models [10], which are used to support of current and future satellite missions, including Athena. In this paper we report on the broad-band energy resolution and uniformity properties of the full 8-column by 32-row system.

II. DETECTOR AND READOUT DESIGN

A. Transition-Edge Sensor and Array Design

The Mo/Au TESs we are using as the baseline for X-IFU differs from previous generations under study in two important ways [2], [11]. Firstly, we have reduced the side length of square TES from $\geq 100 \mu\text{m}$ to $50 \mu\text{m}$, and secondly, we have removed the perpendicular normal metal stripes used atop the sensor for transition shape and noise control. Our previous designs were significantly faster than necessary to achieve the desired X-IFU count-rate requirement, which was in-turn more constraining on the read-out design. These pixels also suffered from localized regions in the current and temperature dependent resistive transition, $R(I, T)$, where the normalized derivatives $\alpha = T/R \partial R/\partial T|_I$ and $\beta = I/R \partial R/\partial I|_T$ would become extremely large. These transition ‘kinks’ can impact performance and affect uniformity in large format arrays (higher ‘excess’ detector noise and introduce significant non-linearity) [11]–[13]. In TDM readout, we electrically bias a column of TESs with a single common applied voltage. Thus, to achieve the desired ΔE_{FWHM} uniformity when common biased we require a high degree of transition-shape uniformity. Our studies on the role of stripes in Mo/Au bilayer TESs suggest they greatly complicate the physics of the device (introducing inhomogeneity in the current and magnetic field distribution), which can make them more susceptible to additional structure in the transition. The smaller TES sizes without metal stripes have established a region of parameter space that seems less susceptible to the kinks [13], [14]. In the 2-d ballistic phonon limit the thermal conductance to the heat-bath G_b scales linearly with the perimeter of the TES on the SiN. Thus, the smaller TES size has also enabled slower pixels better matched to the bandwidth of the read-out.

We use a $50 \times 50 \mu\text{m}^2$ Mo/Au bilayer TES with a transition temperature of ~ 90 mK. A thin ($0.5 \mu\text{m}$) silicon-nitride membrane provides a weak thermal conductance to the 55 mK heat bath. The normal state resistance of these devices is $R_n \sim 9 \text{ m}\Omega$. Detailed characterization of a single pixel TES of this same geometry (including α , β and noise spectra) can be found in [14]. In our prototype kilo-pixel arrays the pixels are fabricated on $250 \mu\text{m}$ pitch (slightly less than the $275 \mu\text{m}$ assumed for X-IFU). The electroplated absorbers measure $240 \times 240 \mu\text{m}^2$ with thickness $1.84 \mu\text{m}$ Au + $3.13 \mu\text{m}$ Bi. The

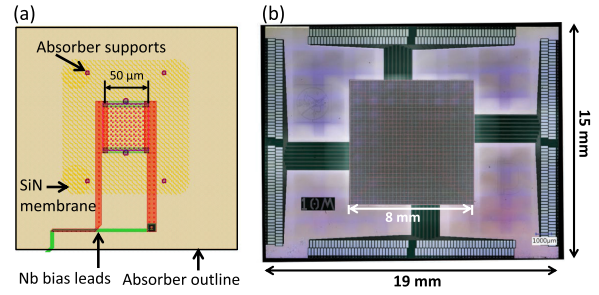


Fig. 1. (a) Schematic of TES pixel design. (b) Photograph of a kilo-pixel array. 252 pixels are connected to the bond-pads around the edge of the chip.

Au layer provides thermal diffusion of the X-ray energy to the TES and the Bi layer provides additional X-ray stopping power without adding significant heat capacity. The total heat-capacity is $C = 0.72 \text{ pJ/K}$, which is dominated by the Au absorber layer. The absorbers are cantilevered $\sim 4.0 \mu\text{m}$ above the TES and membrane, using 6 pillar-shaped supports. Two of these pillars (of $5 \mu\text{m}$ diameter) make contact at the edges of the TES and provide a strong thermal connection to the TES. The 4 additional pillars (of $4 \mu\text{m}$ diameter) are positioned in the corners of the membrane to provide further structural support. Fig. 1a shows the layout of the TES pixel and Fig. 1b shows a photograph of a kilo-pixel array. In this prototype, all the pixels are wired within the interior of the array, and 252 pixels are further routed to the bond-pads around the edge of the chip.

Typically, a large inductance (L_{crit}) is used in series with the TES to critically damp its response, slowing the rise of the pulse (parameterized by the maximum change in current in the TES circuit $dI/dt|_{\text{max}}$, or ‘slew-rate’) and reducing the dynamic range requirement for the readout. For these devices we have found that the responsivity can become extremely non-linear when operated close to critical damping, which in-turn degrades ΔE_{FWHM} . We have empirically found that operating with a total inductance of $L = 0.65 L_{\text{crit}}$, whilst biasing at $\sim 0.1 R_n$, provides a combination of sufficient detector linearity with sufficiently reduced slew-rate to provide optimum ΔE_{FWHM} when readout with TDM.

B. TDM Read-Out Design

The mutual input inductance M_{in} , between the current in the TES circuit and the flux at the SQ1, is an important design parameter that trades the TES referred white readout noise floor with the maximum allowable flux excursion at the SQ1 input. In order to maintain stable FLL operation we require:

$$\Delta\Phi = \frac{dI}{dt}|_{\text{max}} M_{\text{in}} N_{\text{row}} t_{\text{row}} \leq \Delta\Phi_{\text{max}} \quad (1)$$

where $\Delta\Phi$ is the flux excursion from the lock-point and $\Delta\Phi_{\text{max}} \approx 0.3\Phi_0$ is the maximum usable linear flux range of the SQ1. The row-time, t_{row} , is the time each SQ1 is activated before switching to the next, which for X-IFU is 160 ns. In [7], using TDM chips referred to as ‘mux18b’, we designed $M_{\text{in}} = 277 \text{ pH}$. This was optimized to accommodate the peak slew-rate from 12 keV photons with $dI/dt|_{\text{max}} \sim 0.3 \text{ A/s}$ (the largest energy of interest for X-IFU), whilst multiplexing $N_{\text{row}} = 40$. Since 2018, the X-IFU baseline configuration has been reduced to 34 rows in a column. Thus, in our latest experiments we have operated the system in its natural 32-row mode as opposed to

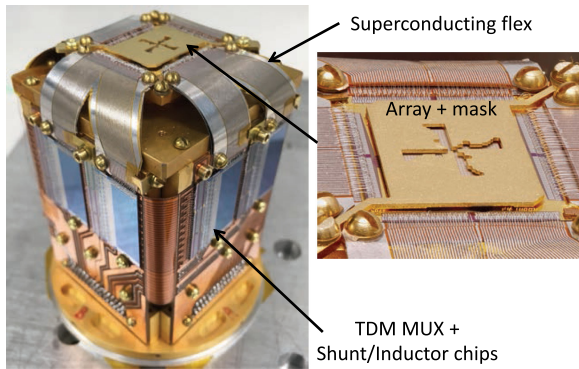


Fig. 2. Shown *left* is a photograph of the 252-pixel detector assembly, read out by 8-column by 32-row TDM. The detector sits atop the assembly, connecting to the side panel via Kapton flex with superconducting Al traces. Each side panel houses the TES bias and TDM readout circuitry for 2 columns. Shown *right* (credit: D.R. Schmidt (NIST)) is a zoom-in of the array and X-ray mask, used to block photons from pixels not connected to bond pads.

the pseudo-40-row mode in [7]. In TDM, the broadband white readout noise level scales with the square root of the number of rows ($\sqrt{N_{\text{row}}}$) [15]. Thus, we would naively expect the readout noise to be reduced from the 25.6 pA/ $\sqrt{\text{Hz}}$ that we reported in our previous 40-row experiments [7] to 22.9 pA/ $\sqrt{\text{Hz}}$ for 32 rows. However, improved filtering of the cryostat feedthrough lines in combination with optimized SQUID design parameters (higher junction critical current and higher junction shunt resistance [4]) has enabled us to now achieve 20.2 pA/ $\sqrt{\text{Hz}}$ in these new 32-row measurements. Further improvements in readout noise for X-IFU are likely when the SQ1 M_{in} coupling is re-optimized from 40-row TDM to 34-row TDM. Additional improvements to the dynamic properties of the readout chain have been made to increase the bandwidth and significantly reduce the malign effects of settling transients due to the fast signals used to switch between rows. This can affect the stability of the FLL and degrade the readout noise during large flux excursions from X-ray pulses. Various sources of electrical crosstalk, both within a column and across multiple columns have also been reduced. The reduction in cross-column crosstalk is critical to scale the system beyond 8 TDM columns. Details of these TDM design optimizations are discussed in [4]. The new multiplexer chips we use here are referred to as ‘mux19a’ and have a measured $M_{\text{in}} = 264$ pH, similar to ‘mux18b’.

The total number of pixels able to be read out was 218 out of the maximum available 252. The missing pixels were predominantly due to defects in the TES bias loop circuitry between the TES and the SQ1 input, including wire bonds and superconducting flexible circuitry. Additionally, one SQ1 row address line was open, which lead to a loss of eight pixels. Experiments were carried out in a He³/He⁴ backed adiabatic magnetization refrigerator (ADR). The 55 mK experimental stage is an 8-column by 32-row ‘snout’ package developed at NIST (see Fig. 2) [16]. The second stage SSAs are situated on the 3 K temperature stage of the ADR.

III. RESULTS AND ANALYSIS

A. Transition Uniformity

To examine the transition shape and uniformity in the array we measured the TES $I(V)$ curves in multiple TDM columns. Fig. 3a shows the $R(T)$ curves across the bias path derived from the

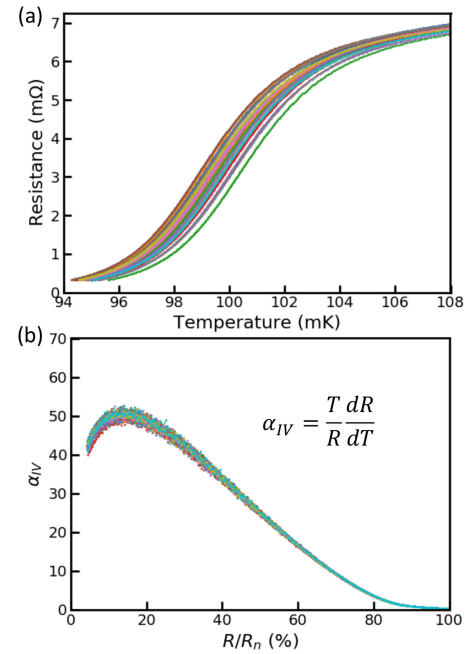


Fig. 3. (a) Resistance versus temperature curves for 30 pixels in a single TDM column. (b) α_{IV} versus R/R_n for the same 30 pixels. The 30 pixels are largely indistinguishable from each other.

power balance equation $I^2 R = G_b(T^n - T_b^n)/(nT^{n-1})$. The thermal conductance on a single representative device was measured to be $G_b = 79$ pW/K (with a temperature exponent of $n = 3.45$). The $I(V)$ curves are analyzed assuming an identical single shunt resistor value ($65 \mu\Omega$) for all pixels. The ADR bath temperature was $T_b = 53.7$ mK. Data are shown for a single representative column of pixels that span the center to edge of the array on one side of the detector. Fig. 3b shows the $\alpha_{IV} = T/R \cdot dR/dT$ as a function of R/R_n for the same 30 pixels. The ~ 2 mK variation in T_C is likely due to intrinsic variations in the Mo/Au bilayer thickness over the array. Importantly, the α_{IV} data are almost indistinguishable from each other and show no evidence of fine structure in the R-T curves such as ‘kinks’, which manifest as large spikes in α_{IV} . This is critical for achieving uniform pulse and noise properties in large arrays.

B. Broadband Energy Resolution

The TES voltage bias for each column was adjusted to bias its TESs at an average operating resistance of 10% R_n . We found this gave slightly better performance compared to original 40-row measurements of [7], which were taken at 11-12% R_n , whilst still being consistent with the maximum slew-rate requirement of ~ 0.3 A/s for 12 keV X-rays. The high degree of uniformity of both the TES transition properties and the bias circuit shunt resistors meant that the standard deviation of the average bias point was $< \pm 0.22\%$ R/R_n over the eight columns. This level of bias uniformity is well within the required specifications for X-IFU.

We measured X-rays from a fluoresced-target source. Separate spectral measurements were taken using high purity Ti, Mn, Co and Cu disks and a KBr crystal. Measurements were taken with an input count-rate of ~ 0.25 cps/pixel. Pulse data records were 41.9 ms long (8192 samples). As in [7], targeted coincidence cuts removed specific victim-perpetrator crosstalk pairs.

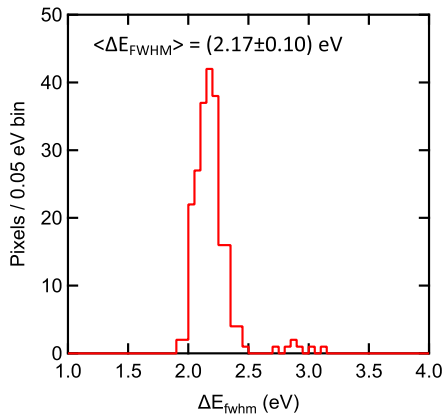


Fig. 4. Histogram of ΔE_{FWHM} , measured at Co-K α (6.9 keV), for all 218 pixels that generated spectra in the array. The average of resolution of pixels in the main distribution is $\langle \Delta E_{FWHM} \rangle = (2.17 \pm 0.10) \text{ eV}$.

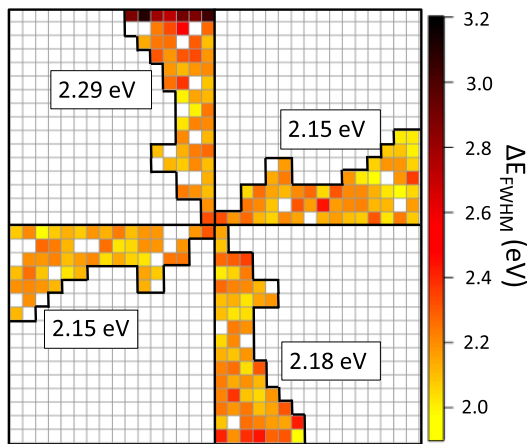


Fig. 5. ΔE_{FWHM} array heat map measured at Co-K α . The region of 63 pixels in each quadrant of the array that connect to the bond-pads are outlined. The average ΔE_{FWHM} obtained in each quadrant is indicated on the figure. The top row of the detector suffered from excess broadening of the intrinsic detector ΔE_{FWHM} due to an absorber fabrication issue.

For all data sets $<5\%$ of events were rejected. The crosstalk levels are consistent with the X-IFU requirements.

For each of the 218 TES pixels that produced X-ray pulses, each triggered data record is digitally processed via the standard optimal-filter technique [17]. Histogrammed spectra of filtered pulse heights are then converted to energy via the recognition of known emission lines. The photon energies are corrected for uncertainty in the pulse arrival phase with respect to the filter template due to trigger jitter. Additional corrections are made to each pixel individually to account for drifts in the detector gains over time (of typically a few eV). The resulting energy histogram is fitted to the assumed line profile for each K α complex to determine the Gaussian energy response of the TES pixel with the best-fit value of ΔE_{FWHM} . A linear local gain slope parameter is included in the fitting routine to account for non-linearity in the energy gain scale. Fig. 4 shows the histogrammed energy resolutions of the 218 TES pixels at the Co-K α complex (6.9 keV). Excluding the seven outlier pixels between $\Delta E_{FWHM} = 2.7$ and 3.2 eV the mean resolution is $\langle \Delta E_{FWHM} \rangle = (2.17 \pm 0.10) \text{ eV}$. The standard

deviation is similar to the average deviation obtained on the fitted ΔE_{FWHM} for each individual pixel ($\pm 0.09 \text{ eV}$). This suggests that the width of the distribution in Fig. 4 (excluding outliers) is dominated by counting statistics and the intrinsic resolution uniformity may be significantly better.

Fig. 5 shows a heat map of ΔE_{FWHM} over the array. The outlier pixels are located in the top physical row of the array. The average measured pulse shapes for these pixels also showed an anomalous, $\sim 10 \text{ ms}$ long, secondary decay time constant, suggesting more complex thermal behavior. Although this affect is not fully understood, it is likely related to improper thermalization of the photon energy in the Bi/Au. This particular wafer used an experimental electroplating recipe, which we believe caused this excess broadening in the intrinsic detector ΔE_{FWHM} . This recipe was subsequently discontinued, and the electroplating process has more generally been optimized to achieve higher quality Bi/Au films. This anomalous behavior has not been seen in our devices since. The second and third row from the top of the detector also showed similar characteristics in the pulse shape and some evidence of broadened ΔE_{FWHM} , albeit to a much lower level.

By coadding the individual gain corrected histograms for each pixel we can also obtain the fitted ΔE_{FWHM} for the array as a whole. Fig. 6(a-e) shows the coadded energy histograms for the five different K α fluorescent line complexes studied. The top row of seven pixels that exhibited excess broadening have been omitted (though, including these pixels only degrades the coadded ΔE_{FWHM} by $\sim 0.03 \text{ eV}$). In addition, seven pixels had significantly faster rise-times than the others. This is thought to be due to defects in the Nyquist inductor coils in the TES bias circuit resulting in lower total inductance. These pixels could be read out for energies $\leq 8 \text{ keV}$ (Cu-K α). However, at Br-K α the larger slew-rates of five of these pixels could not be accurately tracked by the digital FLL. Thus, these pixels were rejected. Three of these same pixels were also removed from the Mn-K α dataset because the gain of the FLL was not properly optimized for those pixels on that data acquisition. The achieved best fit ΔE_{FWHM} for each line is then: 1.94 eV for Ti-K α , 1.97 eV for Mn-K α , 2.16 eV for Co-K α , 2.33 eV for Cu-K α , 3.26 eV for Br-K α . The 1 sigma statistical error is $\leq 0.01 \text{ eV}$ for all spectra.

Since the broadband white readout noise level scales with $\sqrt{N_{\text{row}}}$, to assess the pixel ΔE_{FWHM} in the limit of low readout noise, we have carried out a series of measurements with $N_{\text{row}} = 4$. In this limit the white noise was between 8-10 pA/ $\sqrt{\text{Hz}}$ and we estimate contributes $\sim 1\%$ to the total ΔE_{FWHM} . Testing a subset of 128 representative pixels at Co-K α (excluding the outlier pixels with known absorber issues) we found $\langle \Delta E_{FWHM} \rangle = (2.03 \pm 0.14) \text{ eV}$. This suggests the multiplexed noise penalty when increasing to $N_{\text{row}} = 32$ is approximately 0.1 eV.

Fig. 6(f) shows ΔE_{FWHM} as a function of energy for both the original 40-row measurements of [7] and the 8-column by 32-row results reported here. The improvements in broadband ΔE_{FWHM} are attributed to the lower total readout noise, improvements in the dynamic behavior of the readout chain, and a more optimized TES bias point. The dashed black line in Fig. 6(f) shows the ΔE_{FWHM} requirements for X-IFU, which require 2.5 eV up to 7 keV and 10 eV at 5 eV. It is currently assumed, however, that in order to allow for performance margin and considering noise sources only related to the detector and readout subsystem we require $< 2.24 \text{ eV}$ at energies up to 7 keV (shown by the dashed blue line). Our results meet these more stringent

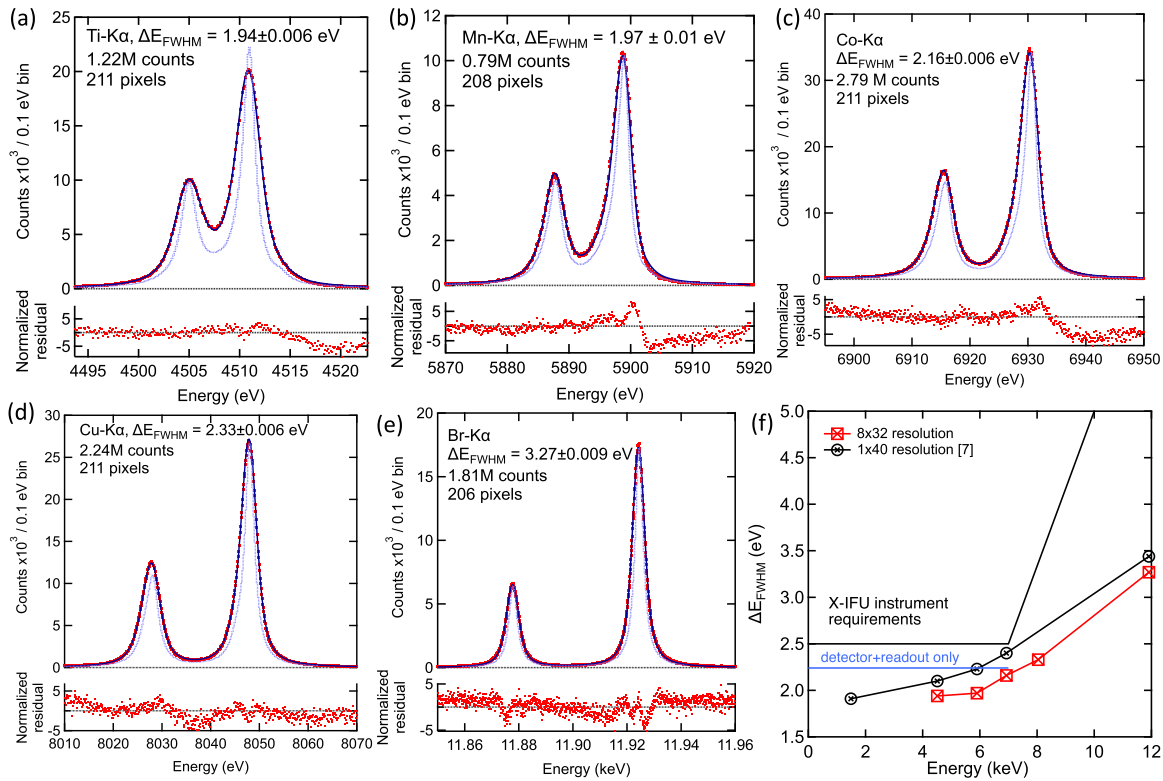


Fig. 6. Coadded 8-column by 32-row spectra for (a) Ti-K α , (b) Mn-K α , (c) Co-K α , (d) Cu-K α and (e) Br-K α (measured from K-Br). The red dots are the data points, the light blue lines are the natural lines shapes and the dark blue line is the fit to data. The fitted ΔE_{FWHM} , number of counts and number of pixels included in each spectrum are shown on the figures. The natural line shapes are from [18] for Ti and [19] for Mn, Co and Cu (we note that using the alternative line shape profile of [20] to fit Cu- K α gives a slightly different best fit resolution of $\Delta E_{FWHM} = 2.42$ eV). The Br line shape is derived from [21], [22], however the α_1/α_2 peak intensities are re-normalized to account for the change in the Au absorber transmission at 11919 eV due to the L_{III} Au absorption edge. (f) ΔE_{FWHM} as a function of energy for the 1-column by 40-row measurements in [7] (black circles) and the new 8-column by 32-row results (red squares). The improved ΔE_{FWHM} is attributed to lower noise, improvements in the dynamic behavior of the readout chain and more optimized TES bias point. The dashed black line shows the X-IFU instrument level resolution requirements, and the dashed blue line shows the currently assumed requirements considering only the detector and readout subsystem and excluding margin.

requirements with some margin at 7 keV and substantial margin for <7 keV.

The final ΔE_{FWHM} margin requirements for X-IFU are yet to be confirmed. However, noting that M_{in} for the current multiplexer chips was designed to accommodate 12 keV photon slew-rates for $N_{row} = 40$, we have some margin in the dynamic range to re-optimize M_{in} for the current baseline of $N_{row} = 34$. Using 1 to re-scale M_{in} to 34-row TDM, we predict the noise would be reduced to $17.7 \text{ pA}/\sqrt{\text{Hz}}$ and gain further resolution margin (we estimate this would improve ΔE_{FWHM} by 0.02 eV).

IV. CONCLUSION

We have demonstrated 8-column by 32-row TDM readout of > 200 pixels in a prototype kilo-pixel array. Our results meet the energy-range and resolution requirements for Athena X-IFU. This laboratory instrument will now be calibrated and delivered to LLNL EBIT for laboratory astrophysics experiments. For X-IFU we are now fabricating full-scale 3168-pixel arrays and developing the infrastructure to test all pixels with TDM readout.

REFERENCES

- [1] D. Barret *et al.*, "The athena X-ray integral field unit (X-IFU)," in *Proc. SPIE Space Telescopes Instrum. Ultraviolet Gamma Ray*, 2016, Art. no. 99052F.
- [2] S. J. Smith *et al.*, "Transition-edge sensor pixel parameter design of the microcalorimeter array for the X-ray integral field unit on athena," in *Proc. vol. 9905, Space Telescopes Instrum. Ultraviolet Gamma Ray*, 2016, Art. no. 99052H.
- [3] W. B. Doriese *et al.*, "Developments in time-division multiplexing of X-ray transition-edge sensors," *J. Low Temp. Phys.*, vol. 184, pp. 389–395, 2016.
- [4] M. Durkin *et al.*, "Mitigating finite bandwidth effects in time-division-multiplexed SQUID readout of TES arrays," *IEEE Trans. Appl. Supercond.*, submitted for publication.
- [5] J. S. Adams *et al.*, "First operation of TES microcalorimeters in space with the Micro-X sounding rocket," *J. Low Temp. Phys.*, vol. 199, pp. 1062–1071, 2020.
- [6] R. P. Welty and J. M. Martinis, "Two-stage integrated SQUID amplifier with series array output," *IEEE Trans. Appl. Supercond.*, vol. 3, no. 1, pp. 2605–2608, Mar. 1993.
- [7] M. Durkin *et al.*, "Demonstration of athena X-IFU compatible 40-row time-division-multiplexed readout," *IEEE Trans. Appl. Supercond.*, vol. 29, no. 5, Aug. 2019, Art. no. 2101005.
- [8] G. V. Brown *et al.*, "A brief overview of the fusion and astrophysics data and diagnostic calibration facility," in *Proc. SPIE 7732, Space Telescopes Instrum. Ultraviolet Gamma Ray*, Jul. 29, 2010, Art. no. 77324Q, [Online]. Available: <https://doi.org/10.1117/12.857555>
- [9] G. L. Betancourt-Martinez *et al.*, "The transition-edge EBIT microcalorimeter spectrometer," in *Proc. Space Telescopes Instrum. Ultraviolet Gamma Ray*, 2014, Art. no. 91443U, [Online]. Available: <https://doi.org/10.1117/12.2055568>
- [10] H. Collaboration, "Atomic data and spectral modeling constraints from high-resolution X-ray observations of the perseus cluster with Hitomi," *Pub. Astronomical Soc. Jpn.*, vol. 70, no. 2, Mar. 12. 2018, [Online]. Available: <https://doi.org/10.1093/pasj/psx156>

- [11] S. J. Smith *et al.*, "Uniformity of kilo-pixel arrays of transition-edge sensor microcalorimeters for X-ray astronomy applications," *IEEE Trans. Appl. Supercond.*, vol. 25, no. 3, Jun. 2015, Art. no. 2100505.
- [12] S. J. Smith *et al.*, "Implications of weak-link behavior on the performance of Mo/Au bilayer transition-edge sensors," *J. Appl. Phys.*, vol. 115, 2013, Art. no. 074513.
- [13] N. A. Wakeham *et al.*, "Effects of normal metal features on superconducting transition-edge sensors," *J. Low Temp. Phys.*, vol. 193, pp. 231–240, 2018.
- [14] A. R. Miniussi *et al.*, "Performance of an X-ray microcalorimeter with a 240 μm absorber and a 50 μm TES bilayer," *J. Low Temp. Phys.*, vol. 193, pp. 337–343, 2018.
- [15] W. B. Doriese *et al.*, "Progress toward kilopixel arrays: 3.8 eV microcalorimeter resolution in 8-channel SQUID multiplexer," *Nucl. Instrum. Methods Phys. Res. Sect. A*, vol. 559, no. 2, pp. 808–810, Apr. 2006.
- [16] W. B. Doriese *et al.*, "A practical superconducting-microcalorimeter X-ray spectrometer for beamline and laboratory science," *Rev. Sci. Instrum.*, vol. 88, no. 5, Apr. 2017, Art. no. 053108.
- [17] J. W. Fowler *et al.*, "The practice of pulse processing," *J. Low Temp. Phys.*, vol. 184, pp. 374–381, 2016. [Online]. Available: <https://doi.org/10.1007/s10909-015-1380-0>
- [18] C. T. Chantler, M. N. Kinnane, C.-H. Su, and J. A. Kimpton, "Characterization of $k\alpha$ spectral profiles for vanadium, component redetermination for scandium, titanium, chromium, and manganese, and development of satellite structure for $z = 21$ to $z = 25$," *Phys. Rev. A*, vol. 73, no. 1, Jan. 2006, Art. no. 012508.
- [19] G. Hölzer, M. Fritsch, M. Deutsch, J. Härtwig, and E. Förster, " $K\alpha_{1,2}$ and $K\beta_1$, 3 X-ray emission lines of the 3d transition metals," *Phys. Rev. A*, vol. 56, no. 6, pp. 4554–4568, Dec. 1997.
- [20] M. H. Mendenhall, A. Henins, L. T. Hudson, C. I. Szabo, D. Windover, and J. P. Cline, "High-precision measurement of the X-ray Cu $k\alpha$ spectrum," *J. Phys. B: At, Mol. Opt. Phys.*, vol. 50, no. 11, 2017, Art. no. 115004.
- [21] M. O. Krause and J. H. Oliver, "Natural widths of atomic K and L levels, $k\alpha$ X-ray lines and several KLL auger lines," *J. Phys. Chem. Ref. Data*, vol. 8, no. 2, pp. 329–338, Apr. 1979.
- [22] J. A. Bearden, "X-ray wavelengths," *Rev. Mod. Phys.*, vol. 39, no. 1, pp. 78–174, Jan. 1967.